Supplement of Atmos. Chem. Phys., 26, 7933–7947, 2026
https://doi.org/10.5194/acp-26-7933-2026-supplement

Atmospheric Chemistry and Physics
Open Access
EGU

Supplement of

Satellite observations reveal heterogeneous atmospheric composition responses to rapid emission changes

Zeyu Yang et al.

Correspondence to: Jing Wei (jingwei@pku.edu.cn)

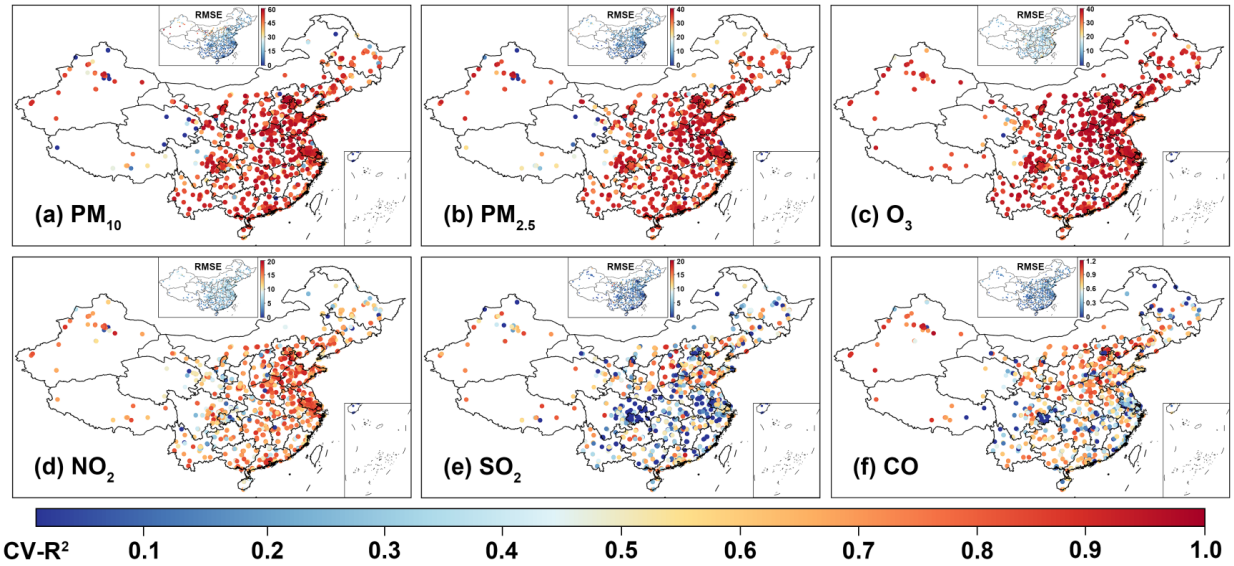

Figure S1. Site-specific overall accuracy of daily air pollutant estimates.
Spatial distributions of sample-based cross-validated (CV) coefficients of determination (R^2) and root-mean-square errors (RMSE) for daily estimates of (a) PM_{10} (μg m^{-3}), (b) $PM_{2.5}$ (μg m^{-3}), (c) O_3 (μg m^{-3}), (d) NO_2 (μg m^{-3}), (e) SO_2 (μg m^{-3}), and (f) CO (mg m^{-3}) compared with ground-based measurements at each Ministry of Ecology and Environment (MEE) monitoring station across China from 2019 to 2022.

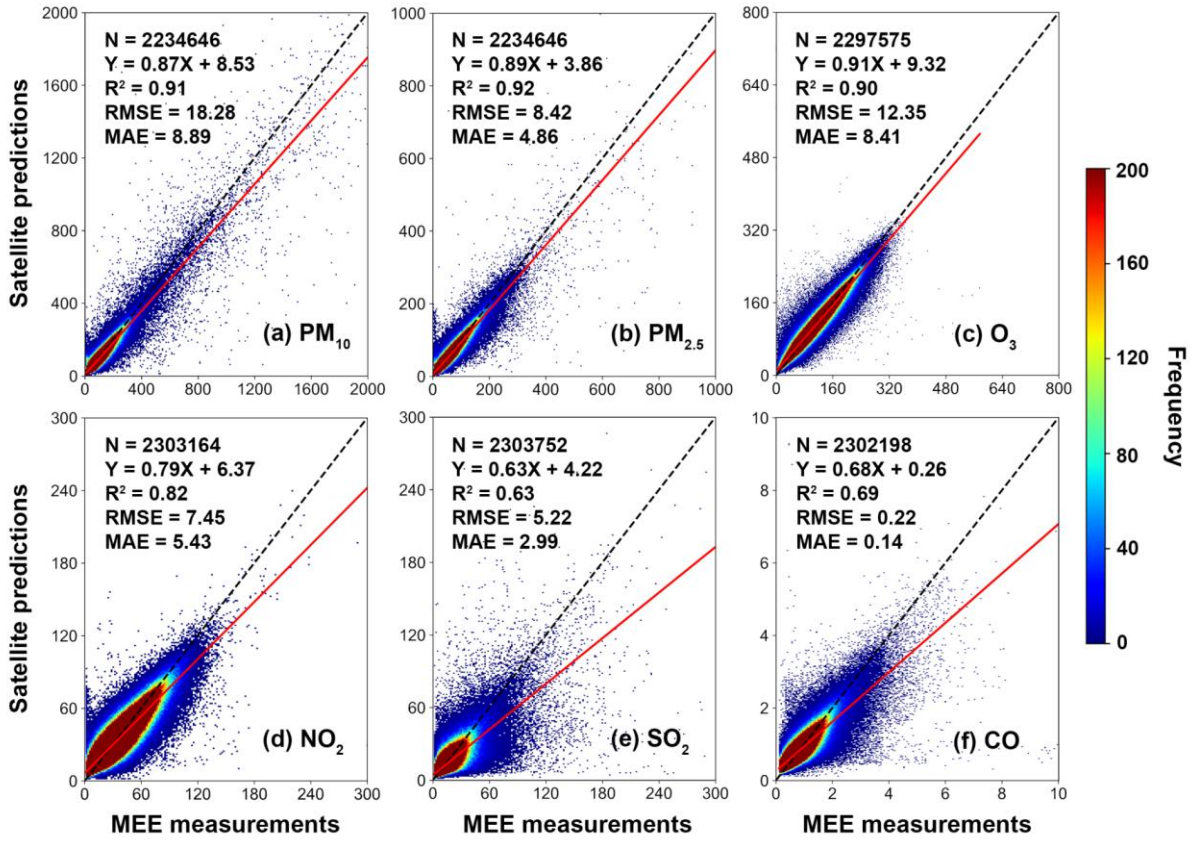

Figure S2. Spatial prediction accuracy of daily air pollutants in China.
Density scatter plots of satellite-derived daily gapless 1 km concentrations of ambient air pollutants—(a) PM_{10} (μg m^{-3}), (b) $PM_{2.5}$ (μg m^{-3}), (c) O_3 (μg m^{-3}), (d) NO_2 (μg m^{-3}), (e) SO_2 (μg m^{-3}), and (f) CO (mg m^{-3}) —using the unified four-dimensional spatiotemporal deep forest (4D-STDF) model against ground-based measurements from all Ministry of Ecology and Environment (MEE) monitoring stations across China from 2019 to 2022, based on station-based 10-fold cross-validation approach. The black dashed lines represent the 1:1 reference lines, while the red lines indicate the best-fit lines derived from linear regression.

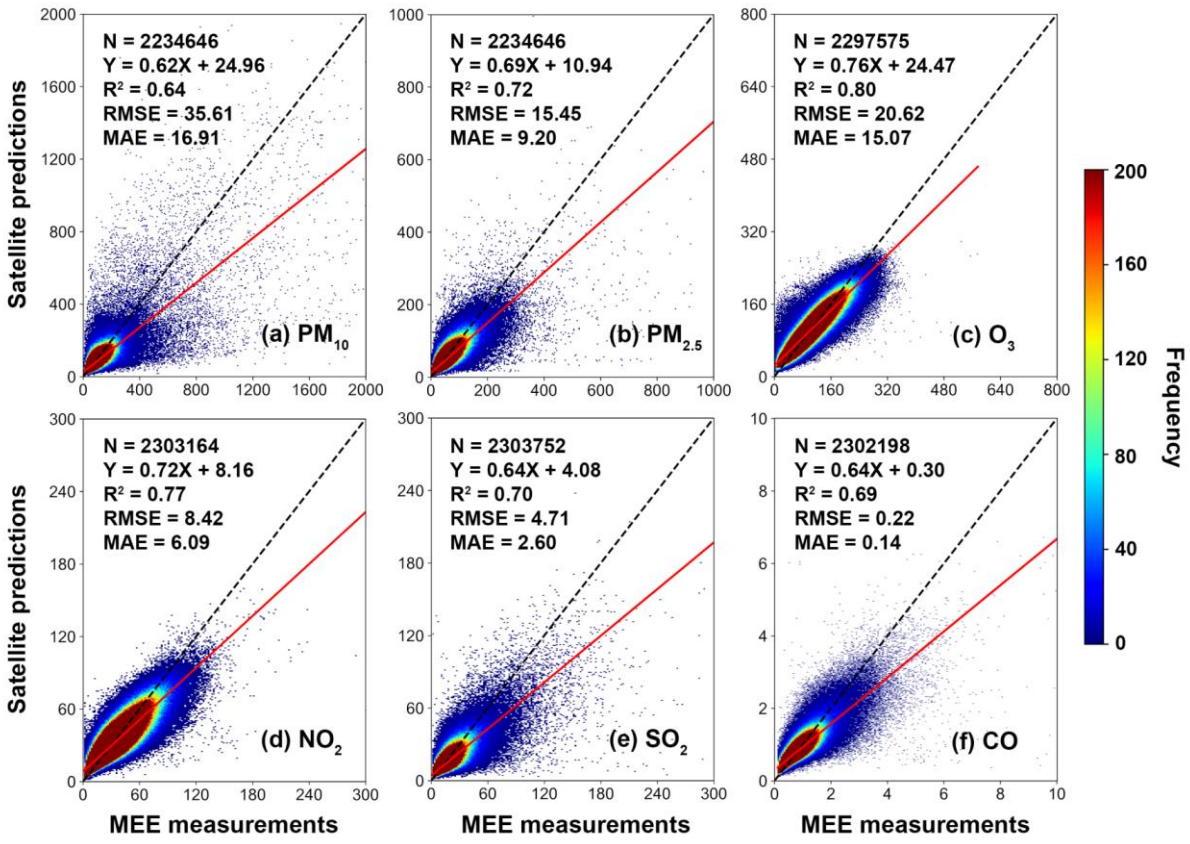

Figure S3. Temporal prediction accuracy of daily air pollutants in China.
Density scatter plots of satellite-derived daily gapless 1 km concentrations of ambient air pollutants—(a) PM_{10} (μg m^{-3}), (b) $PM_{2.5}$ (μg m^{-3}), (c) O_3 (μg m^{-3}), (d) NO_2 (μg m^{-3}), (e) SO_2 (μg m^{-3}), and (f) CO (mg m^{-3}) —using the unified four-dimensional spatiotemporal deep forest (4D-STDF) model against ground-based measurements from all Ministry of Ecology and Environment (MEE) monitoring stations across China from 2019 to 2022, based on day-based 10-fold cross-validation approach. The black dashed lines represent the 1:1 reference lines, while the red lines indicate the best-fit lines derived from linear regression.

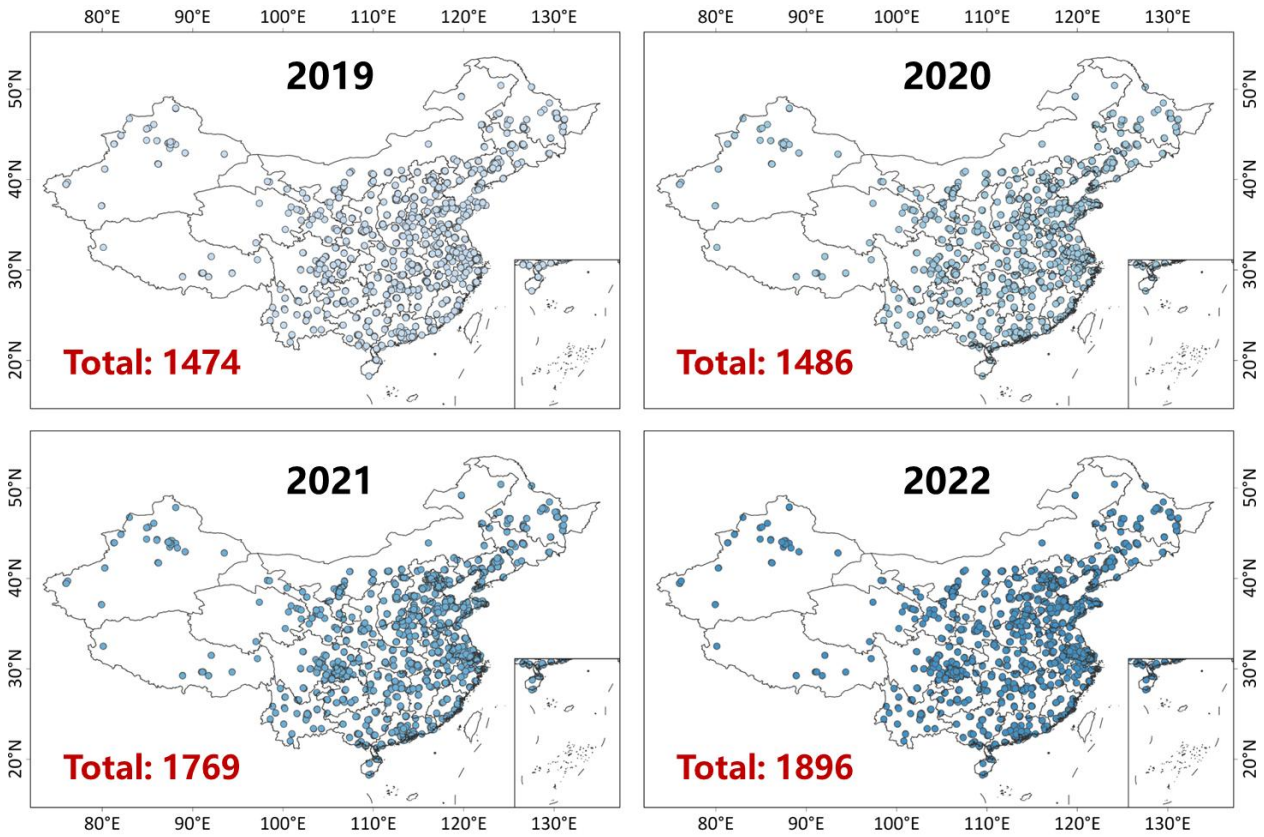

Figure S4. Spatial distribution of monitoring stations in China.
Spatial distribution of ground-based monitoring stations across China from 2019 to 2022. Numbers shown in each panel indicate the total number of stations for the corresponding year.

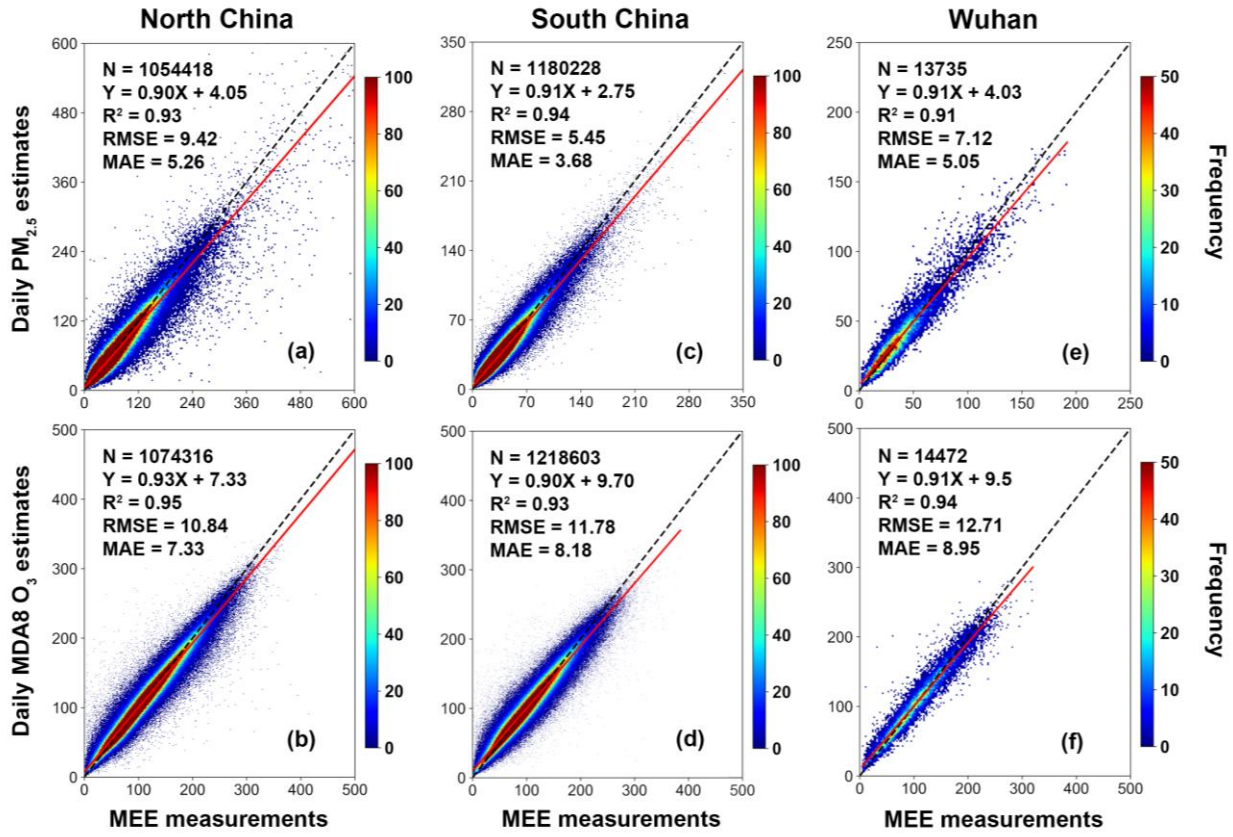

Figure S5. Regional validation of daily surface O_3 estimates.
Density scatter plots of satellite-derived daily concentrations of (a–c) $PM_{2.5}$ (μg m^{-3}) and (d–f) O_3 (μg m^{-3}) from the unified four-dimensional spatiotemporal deep forest (4D-STDF) model against ground-based measurements in Northern China (left), Southern China (middle), and Wuhan (right), based on sample-based cross-validation. The black dashed lines represent the 1:1 reference lines, and the red lines indicate the fitted linear regression lines.

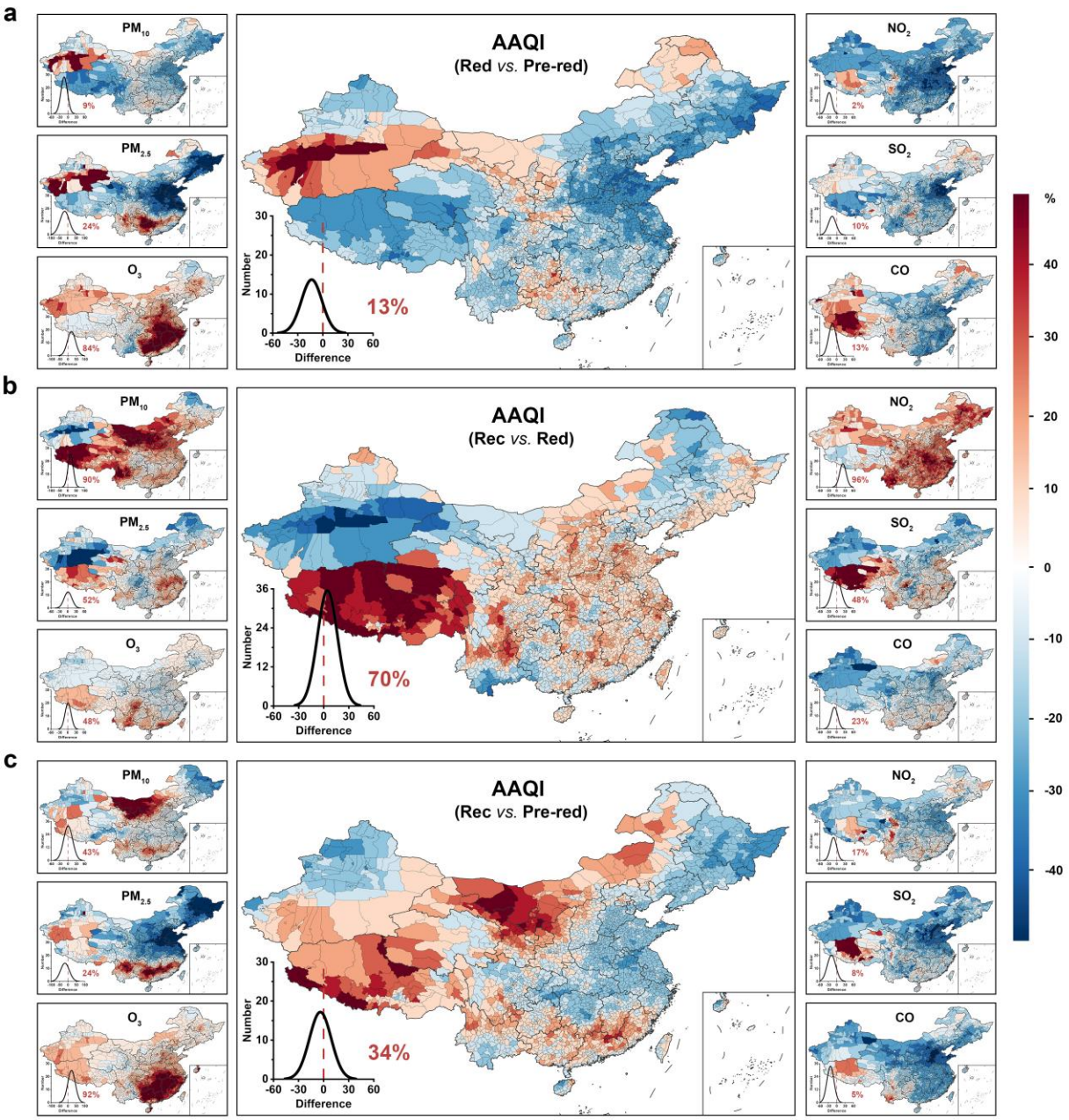

Figure S6. Changes in air pollution across different emission-change eras.
Spatial distributions of relative differences (%) in the Aggregated Air Quality Index (AAQI) and Individual Air Quality Index (IAQI) for PM_{10}, $PM_{2.5}$, O_3, NO_2, SO_2, and CO during the most stringent emission reduction periods, compared across three eras—(a) reduction vs. pre-reduction, (b) recovery vs. reduction, and (c) recovery vs. pre-reduction—at the country level in China. Lower-left plots display frequency histograms, with red numbers indicating the percentage of counties showing deteriorating air quality.

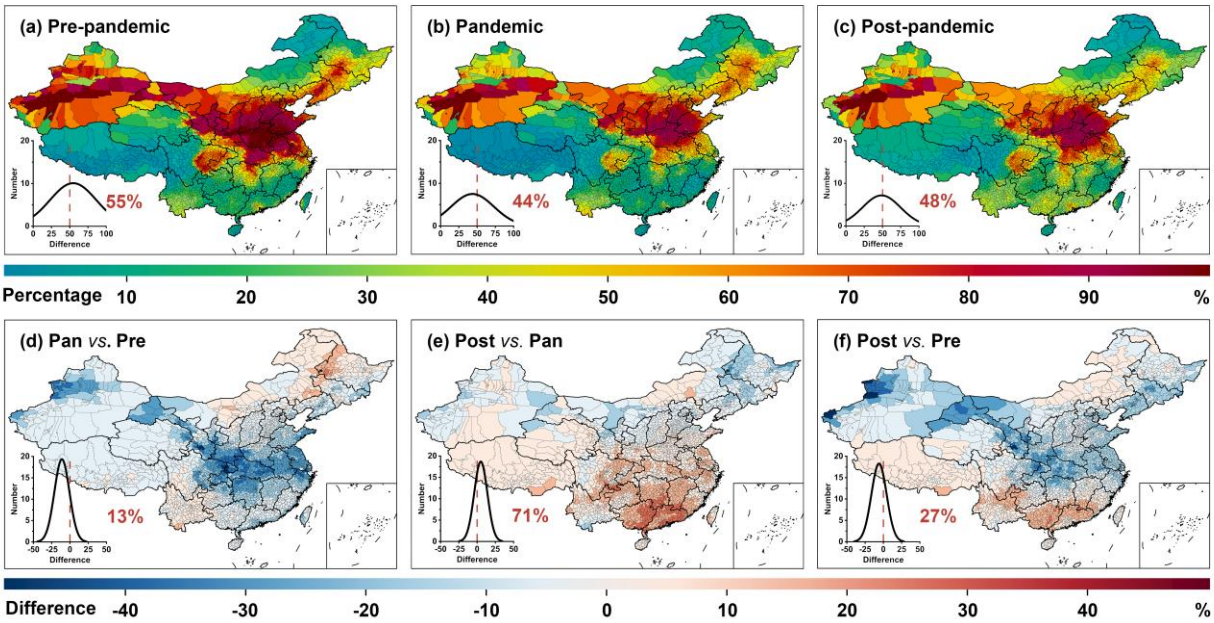

Figure S7. Changes in unhealthy air days across different emission-change eras.
Spatial distribution of the percentage of days exceeding unhealthy air quality levels [i.e., falling outside the Good (AAQI = 0–50) and Moderate (51–100) categories] during the first quarter (January–March) for (a) pre-reduction, (b) reduction, and (c) recovery periods, along with percentage differences for (d) reduction vs. pre-reduction, (e) recovery vs. reduction, and (f) recovery vs. pre-reduction at the country level across China.

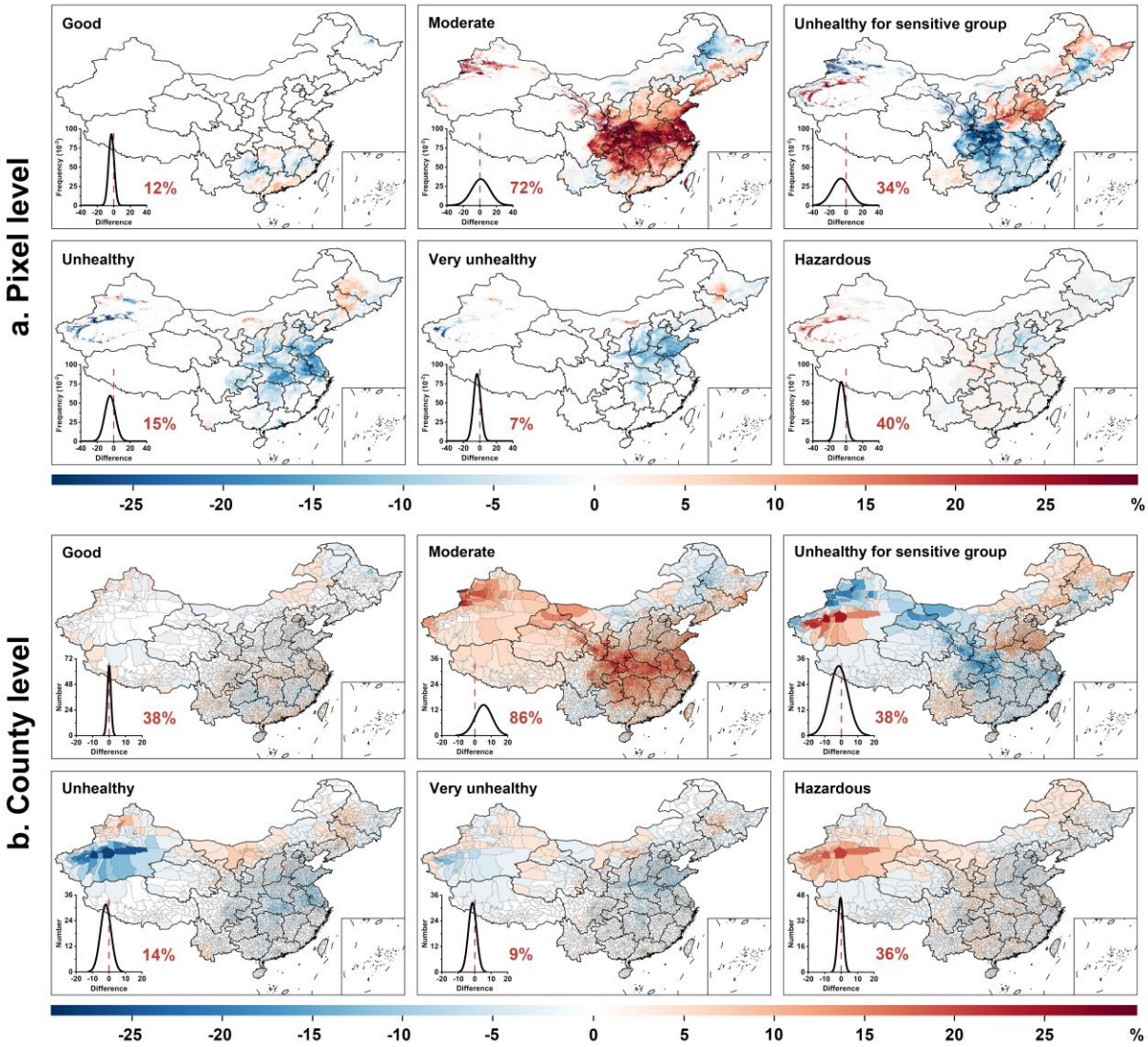

Figure S8. Changes in polluted days between the reduction and pre-reduction periods. Spatial distribution of differences (%) in the number of days exceeding various air quality levels: (a) Good (AQI = 0–50), (b) Moderate (51–100), (c) Unhealthy for Sensitive Groups (101–150), (d) Unhealthy (151–200), (e) Very Unhealthy (201–300), and (f) Hazardous (301–500). Data cover (top) each 1-km^2 grid for inhabited areas (population density > 1 person km^{-2}), and (bottom) the country level across China, comparing air quality between the reduction (2020) and pre-reduction (2019) periods during the first quarter (January–March). Lower-left plots display frequency histograms, with red numbers indicating the percentage of pixels or counties showing positive changes.

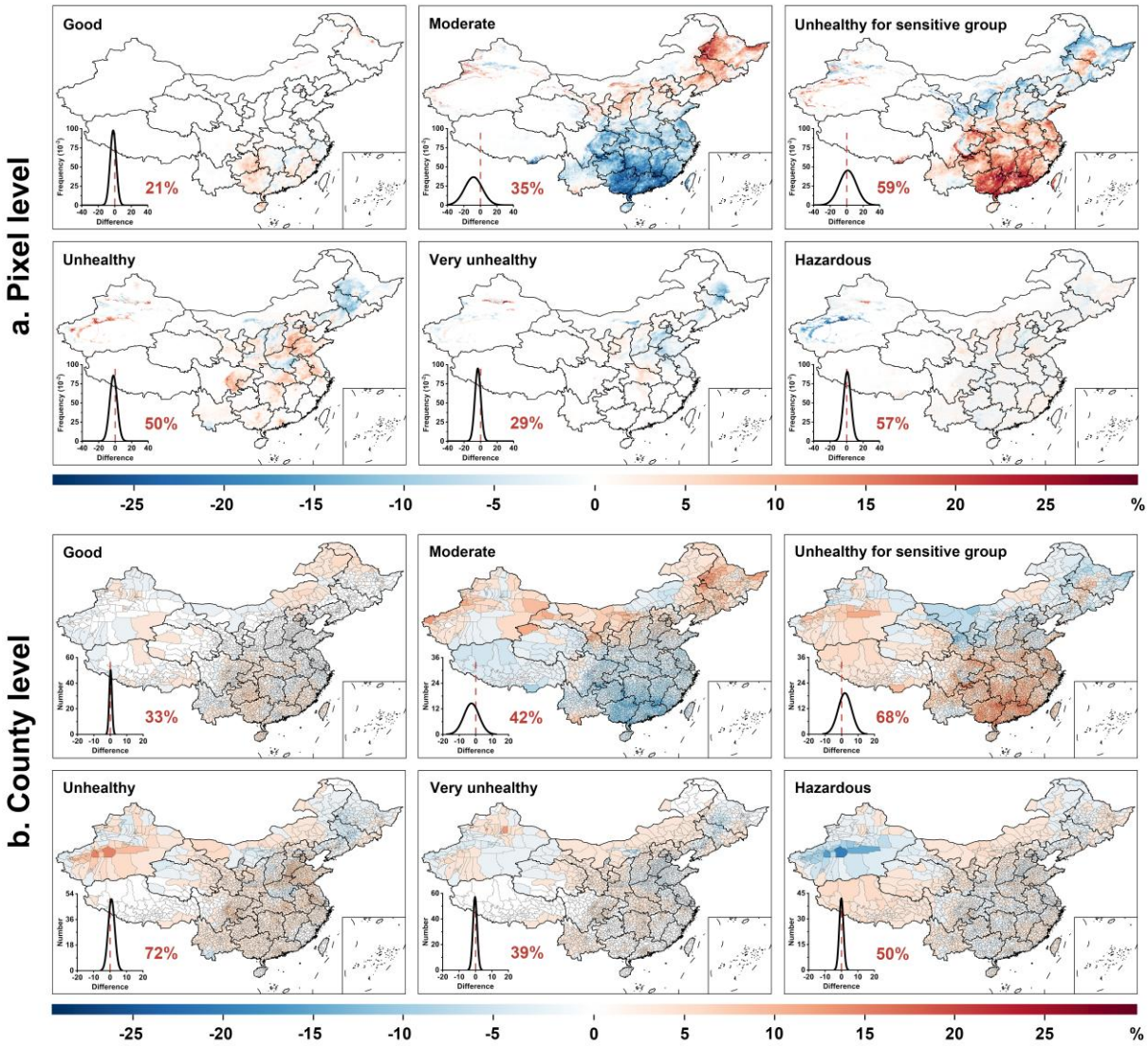

Figure S9. Changes in polluted days between the recovery and reduction periods.
Spatial distribution of differences (%) in the number of days exceeding various air quality levels: (a) Good (AQI = 0–50), (b) Moderate (51–100), (c) Unhealthy for Sensitive Groups (101–150), (d) Unhealthy (151–200), (e) Very Unhealthy (201–300), and (f) Hazardous (301–500). Data cover (top) 1-km^2 grid for inhabited areas (population density > 1 person km^{-2}), and (bottom) the country level across China, comparing air quality between the recovery (2021–2022) and reduction (2020) periods during the first quarter (January–March). Lower-left plots display frequency histograms, with red numbers indicating the percentage of pixels or counties showing positive changes.

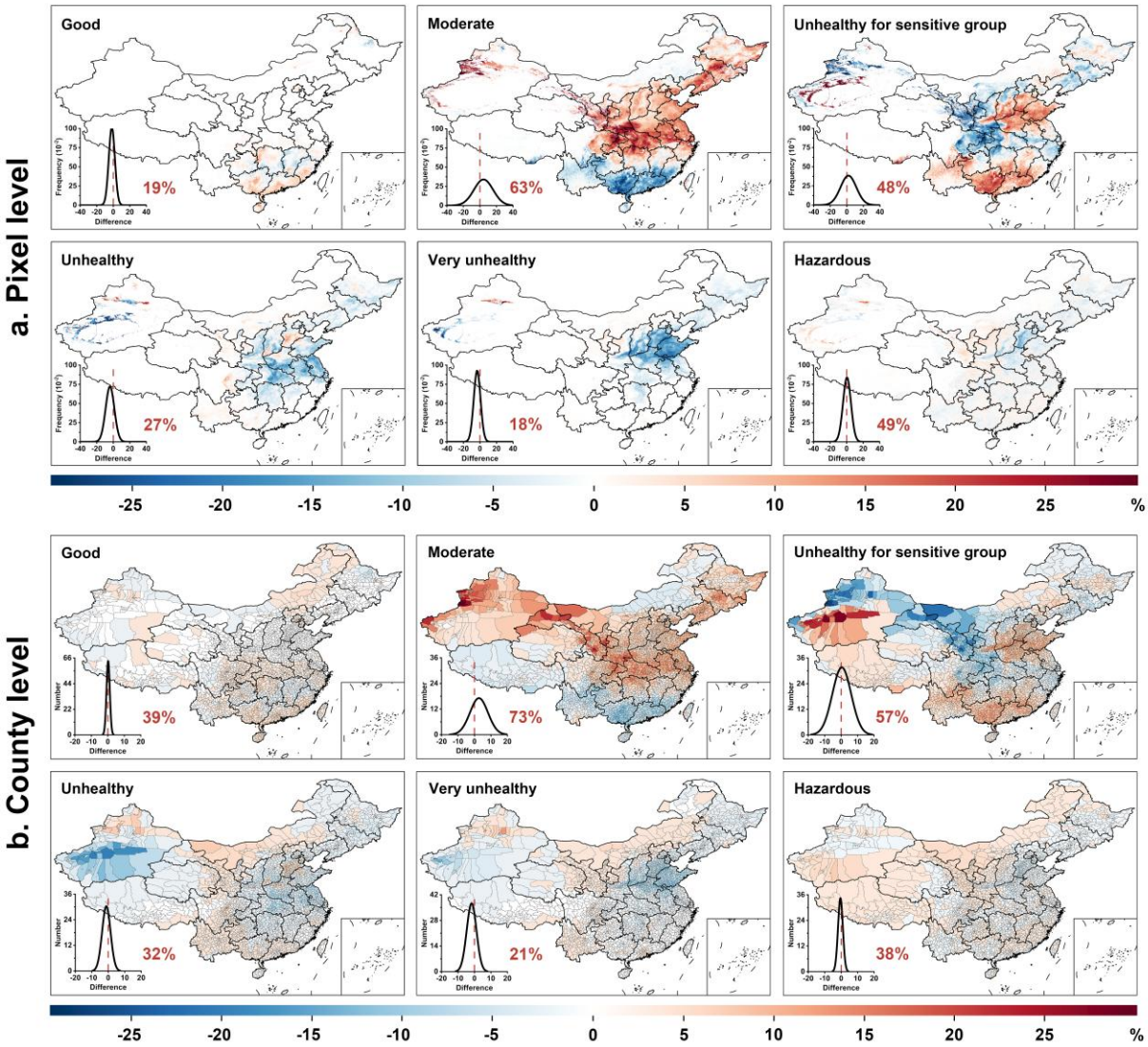

Figure S10. Changes in polluted days between the recovery and pre-reduction periods. Spatial distribution of differences (%) in the number of days exceeding various air quality levels: (a) Good (AQI = 0–50), (b) Moderate (51–100), (c) Unhealthy for Sensitive Groups (101–150), (d) Unhealthy (151–200), (e) Very Unhealthy (201–300), and (f) Hazardous (301–500). Data cover (top) each 1-km^2 grid for inhabited areas (population density > 1 person km^{-2}), and (bottom) the country level across China, comparing air quality between the recovery (2021–2022) and pre-reduction (2019) periods during the first quarter (January–March). Lower-left plots display frequency histograms, with red numbers indicating the percentage of pixels or counties showing positive changes.

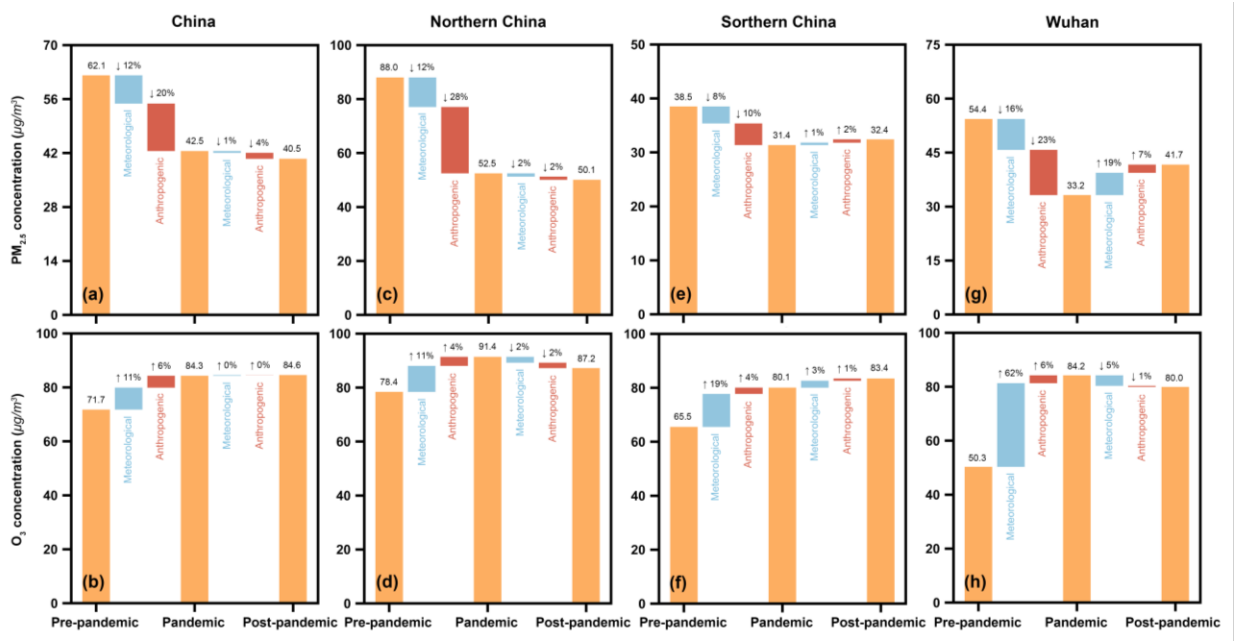

Figure S11. Drivers of air quality variations across different emission-change eras. Influencing factors driving changes in ambient $PM_{2.5}$ and O_3 pollution during the most stringent emission reduction period—from the pre-reduction (2019) to the reduction (2020) and recovery (2021–2022) periods—in (a & b) China, (c & d) Northern China, (e & f) Southern China, and (g & h) Wuhan city, Hubei province, respectively, using the traditional Multiple Linear Regression (MLR) method. The blue and red bars represent the impacts of meteorological conditions and anthropogenic emissions, respectively.

Table S1. Summary of datasets used in air pollutant modeling with deep learning.

Content	Abbreviation	Spatial Resolution	Temporal Resolution	Data Source
Air quality measurements	$PM_{2.5}$, PM_{10}, NO_2, SO_2, O_3	in situ	Hourly	CNEMC (MEE, 2018)
	CO			
MAIAC AOD (550 nm)	AOD	1 km × 1 km	Daily	MCD19A2 (Lyapustin et al., 2018)
Tropospheric NO_2 column	NO_2	1 km × 1 km	Daily	TROPOMI (Veefkind et al., 2012)
Total SO_2 column	SO_2			
Total CO column	CO			
Tropospheric HCHO column	HCHO			
Downward shortwave radiation	DSR	1 km × 1 km	Daily	MCD18A1 (Wang et al., 2020)
Land surface temperature	LST	1 km × 1 km	Daily	MODIS (Zhang et al., 2022)
$PM_{2.5}$ mass simulation	$PM_{2.5}$	0.25° × 0.25°	Hourly	GEOS-CF (Keller et al., 2021)
Surface NO_2 mass simulation	NO_2			
Surface SO_2 mass simulation	SO_2			
Surface CO mass simulation	CO			
Surface O_3 mass simulation	O_3			
PM_{10} mass simulation	MPM_{10}	0.75° × 0.75°	3-hour	CAMS (Inness et al., 2019)
Ammonia	NH_3	1 km × 1 km	Daily	ABaCAS-EI (Li et al., 2023)
Nitrogen oxides	NO_x			
Sulfur dioxide	SO_2			
Carbon monoxide	CO			
Volatile organic compounds	VOCs			
Fine particle	$PM_{2.5}$			
Coarse particle	PM_{10}			
Temperature	TEM	0.1° × 0.1°	Hourly	ERA5 (Hersbach et al., 2020)
U-component of wind	WU			
V-component of wind	WV			
Surface pressure	SP			
Precipitation	TP			
Evaporation	ET			
Boundary-layer height	BLH	0.25° × 0.25°		
Relative humidity	RH			
Population density	POD	1 km × 1 km	Annual	LandScan™ (Dobson et al., 2000)
Nighttime lights	NTL	500 m × 500 m	Monthly	VIIRS (Elvidge et al., 2017)
NDVI	NDVI	1 km × 1 km	Monthly	MOD13A3 (Didan et al., 2015)
Surface elevation	DEM	90 m × 90 m	-	SRTM (Farr et al., 2007)

Table S2. Air Quality Index (AQI) and its descriptions (MEE, 2012).

Levels	Index Value	Description of Air Quality
Good	[0, 50]	Air quality is satisfactory, and air pollution poses little or no risk.
Moderate	(50, 100]	Air quality is acceptable. However, there may be a risk for some people, particularly those sensitive to pollution.
Unhealthy for Sensitive Groups	(100, 150]	Members of sensitive groups may experience health effects. The general public is less likely to be affected.
Unhealthy	(150, 200]	Some members of the general public may experience health effects; sensitive groups may experience more serious effects.
Very Unhealthy	(200, 300]	Health alert: The risk of health effects is increased for everyone.
Hazardous	(300, ∞)	Health warning of emergency conditions: everyone is more likely to be affected.

Table S3. Input variables and Variance Inflation Factor (VIF) values in $PM_{2.5}$ driving analysis.

Category	Variable	China	Northern China	Southern China	Wuhan
Anthropogenic emissions	Carbon monoxide	2.30	2.48	2.02	2.47
	Nitrogen dioxide	4.52	4.16	3.78	2.91
	Sulfur dioxide	5.42	5.28	3.20	4.26
	Volatile Organic Compounds	2.70	2.12	1.99	1.25
Meteorological factors	Air temperature	3.52	5.27	3.94	2.53
	Boundary layer height	2.76	2.62	2.66	2.82
	Relative humidity	4.33	4.08	2.64	1.93
	Surface pressure	1.82	7.19	4.07	2.52
	Total precipitation	1.53	1.41	1.67	1.40
	Wind direction	1.66	1.67	1.72	1.42
	Wind Speed	1.97	1.94	2.00	2.25

Table S4. Input variables and Variance Inflation Factor (VIF) values in O_3 driving analysis.

Category	Variable	China	Northern China	Southern China	Wuhan
Anthropogenic emissions	Carbon monoxide	2.30	2.03	2.06	1.96
	Nitrogen dioxide	2.90	3.01	2.07	1.70
	Volatile Organic Compounds	2.92	2.25	2.06	1.28
Meteorological factors	Air temperature	9.86	1.58	4.49	2.90
	Boundary layer height	2.68	4.07	3.17	2.99
	Downward shortwave radiation	1.85	1.43	1.30	1.50
	Relative humidity	2.77	3.45	3.24	2.29
	Surface pressure	8.79	1.70	4.84	2.81
	Surface sensible heat flux	2.06	2.15	2.14	1.91
	Total cloud cover	1.65	2.23	1.71	1.72
	Total precipitation	1.62	1.70	1.73	1.58
	Wind direction	1.68	1.62	1.83	1.47
	Wind Speed	1.87	2.81	2.08	2.23

Table S5. Year-specific prediction accuracy of daily air pollutants estimates in China.

Variable	Year	Slope	R^2	RMSE	MAE
PM_{10}	2019	0.86	0.91	17.11	9.26
	2020	0.86	0.89	16.64	7.93
	2021	0.89	0.93	20.21	8.06
	2022	0.90	0.93	12.51	6.97
$PM_{2.5}$	2019	0.90	0.93	8.79	5.15
	2020	0.90	0.93	7.97	4.46
	2021	0.90	0.93	7.25	4.22
	2022	0.91	0.94	6.40	4.00
O_3	2019	0.90	0.93	13.59	9.32
	2020	0.91	0.94	11.08	7.68
	2021	0.91	0.94	10.64	7.43
	2022	0.93	0.95	10.11	6.92
NO_2	2019	0.82	0.86	7.19	5.17
	2020	0.83	0.87	6.35	4.54
	2021	0.83	0.87	6.10	4.42
	2022	0.81	0.86	5.8	4.12
SO_2	2019	0.77	0.81	4.87	2.54
	2020	0.74	0.79	4.08	2.14
	2021	0.71	0.77	3.64	1.91
	2022	0.71	0.76	3.13	1.74
CO	2019	0.78	0.82	0.20	0.13
	2020	0.77	0.81	0.18	0.11
	2021	0.72	0.75	0.18	0.11
	2022	0.74	0.78	0.16	0.10

References

Didan, K., Munoz, A. B., Solano, R., and Huete, A.: MODIS vegetation index user's guide (MOD13 series), University of Arizona: vegetation index and Phenology Lab, 35, 2–33, 2015.

Dobson, J. E., Bright, E. A., Coleman, P. R., Durfee, R. C., and Worley, B. A.: LandScan: a global population database for estimating populations at risk, Photogrammetric engineering and remote sensing, 66, 849–857, 2000.

Elvidge, C. D., Baugh, K., Zhizhin, M., Hsu, F. C., and Ghosh, T.: VIIRS night-time lights, International Journal of Remote Sensing, 38, 5860–5879, 2017.

Farr, T. G., Rosen, P. A., Caro, E., Crippen, R., Duren, R., Hensley, S., Kobrick, M., Paller, M., Rodriguez, E., Roth, L., Seal, D., Shaffer, S., Shimada, J., Umland, J., Werner, M., Oskin, M., Burbank, D., and Alsdorf, D.: The Shuttle Radar Topography Mission, Reviews of Geophysics, 45, 2007.

Hersbach, H., Bell, B., Berrisford, P., Hirahara, S., Horányi, A., Muñoz-Sabater, J., Nicolas, J., Peubey, C., Radu, R., Schepers, D., Simmons, A., Soci, C., Abdalla, S., Abellan, X., Balsamo, G., Bechtold, P., Biavati, G., Bidlot, J., Bonavita, M., De Chiara, G., Dahlgren, P., Dee, D., Diamantakis, M., Dragani, R., Flemming, J., Forbes, R., Fuentes, M., Geer, A., Haimberger, L., Healy, S., Hogan, R. J., Hólm, E., Janisková, M., Keeley, S., Laloyaux, P., Lopez, P., Lupu, C., Radnoti, G., de Rosnay, P., Rozum, I., Vamborg, F., Villaume, S., and Thépaut, J.-N.: The ERA5 global reanalysis, Quarterly Journal of the Royal Meteorological Society, 146, 1999–2049, 2020.

Inness, A., Ades, M., Agustí-Panareda, A., Barré, J., Benedictow, A., Blechschmidt, A. M., Dominguez, J. J., Engelen, R., Eskes, H., Flemming, J., Huijnen, V., Jones, L., Kipling, Z., Massart, S., Parrington, M., Peuch, V. H., Razinger, M., Remy, S., Schulz, M., and Suttie, M.: The CAMS reanalysis of atmospheric composition, Atmospheric Chemistry and Physics, 19, 3515–3556, 2019.

Keller, C. A., Knowland, K. E., Duncan, B. N., Liu, J., Anderson, D. C., Das, S., Lucchesi, R. A., Lundgren, E. W., Nicely, J. M., Nielsen, E., Ott, L. E., Saunders, E., Strode, S. A., Wales, P. A., Jacob, D. J., and Pawson, S.: Description of the NASA GEOS Composition Forecast Modeling System GEOS-CF v1.0, Journal of Advances in Modeling Earth Systems, 13, e2020MS002413, 2021.

Li, S., Wang, S., Wu, Q., Zhang, Y., Ouyang, D., Zheng, H., Han, L., Qiu, X., Wen, Y., Liu, M., Jiang, Y., Yin, D., Liu, K., Zhao, B., Zhang, S., Wu, Y., and Hao, J.: Emission trends of air pollutants and CO_2 in China from 2005 to 2021, Earth System Science Data, 15, 2279–2294, 2023.

Lyapustin, A., Wang, Y., Korkin, S., and Huang, D.: MODIS Collection 6 MAIAC algorithm, Atmospheric Measurement Techniques, 11, 5741–5765, 2018.

MEE: Technical Regulation on Ambient Air Quality Index (on trial), 2012.

MEE: Ministry of Ecology and Environment (MEE), 2018. Revision of the Ambien air quality standards (GB 3095–2012) (in Chinese), 2018.

Veefkind, J. P., Aben, I., McMullan, K., Förster, H., de Vries, J., Otter, G., Claas, J., Eskes, H. J.,

de Haan, J. F., Kleipool, Q., van Weele, M., Hasekamp, O., Hoogeveen, R., Landgraf, J., Snel, R., Tol, P., Ingmann, P., Voors, R., Kruizinga, B., Vink, R., Visser, H., and Levelt, P. F.: TROPOMI on the ESA Sentinel-5 Precursor: A GMES mission for global observations of the atmospheric composition for climate, air quality and ozone layer applications, Remote Sensing of Environment, 120, 70–83, 2012.

Wang, D., Liang, S., Zhang, Y., Gao, X., Brown, M. G. L., and Jia, A.: A New Set of MODIS Land Products (MCD18): Downward Shortwave Radiation and Photosynthetically Active Radiation, Remote Sensing, 12, 168, 2020.

Zhang, T., Zhou, Y., Zhu, Z., Li, X., and Asrar, G. R.: A global seamless 1 km resolution daily land surface temperature dataset (2003–2020), Earth System Science Data, 14, 651–664, 10.5194/essd-14-651-2022, 2022.